

# Influence of a bosonic environment onto the non-equilibrium dynamics of local electronic states in a quantum impurity system close to a quantum phase transition

Christian Kleine and Frithjof B. Anders

*Lehrstuhl für Theoretische Physik II, Technische Universität Dortmund,  
Otto-Hahn-Straße 4, 44221 Dortmund, Germany*

(Dated: December 22, 2015)

We investigate the influence of an additional bosonic bath onto the real-time dynamics of a localized orbital coupled to conduction band with an energy-dependent coupling function  $\Gamma(\varepsilon) \propto |\varepsilon|^r$ . Recently, a rich phase diagram has been found in this Bose-Fermi Anderson model, where the transitions between competing ground states are governed by quantum critical points. In addition to a transition between a Kondo singlet and a local moment, a localized phase has been established once the coupling to a sub-ohmic bosonic bath exceeds a critical value. Using the time-dependent numerical renormalization group approach, we show that the non-equilibrium dynamics with F-type of bath exponents can be fully understood within an effective single-impurity Anderson model using a renormalized local Coulomb interaction  $U_{\text{ren}}$ . For regimes with B-type of bath exponents, the nature of the bosonic bath and the coupling strength has a profound impact on the electron dynamics which can only partially be understood using an appropriate  $U_{\text{ren}}$ . The local expectation values always reach a steady state at very long times. By a scaling analysis for  $\Lambda \rightarrow 1^+$ , we find thermalization of the system only in the strong coupling regime. In the local moment and in the localized phase significant deviations between the steady-state value and the thermal equilibrium value are found that are related to the distance to the quantum critical point.

PACS numbers: 05.70.Ln, 72.15.Qm, 78.67.Hc

## I. INTRODUCTION

Quantum impurity systems (QISs) [1] are of great interest for the understanding of nanoscale devices, such as semi-conductor quantum dots, or qubits for quantum computation [2]. These systems consist of a small subsystem with a finite number of degrees of freedom (DOFs), interacting with an infinitely large environment of non-interacting particles. Several classes of models have been investigated with purely fermionic [3–7] or purely bosonic [8–10] environments in the last decades. In many of these models impurity quantum phase transitions (QPTs) have been found and are well understood [11]. In contrary to bulk QPTs [12], only a subset of the DOFs becomes critical in these boundary QPTs [11].

In the last decade one focus has been on mixed Bose-Fermi QISs containing multiple baths of fermionic and bosonic DOFs [11, 13–20] extending some earlier work [21–23]. The spin-1/2 Bose-Fermi Kondo model (BFKM) [15] and its extension to the charge sector, the Bose-Fermi Anderson model (BFAM) [18, 20], are the most studied models. These models can serve as effective site in the extended dynamical mean-field theory (EDMFT) [24, 25] which is used to address the occurrence of magnetic QPTs in heavy fermions [12, 26] and in the Kondo lattice model (KLM) [27, 28]. Hereby, the bosonic parts of the BFAM represent the fluctuating effective magnetic order parameter field generated by the other  $f$  moments. In the KLM the magnetic ordering induced by the Ruderman-Kittel-Kasuya-Yosida (RKKY) interaction [29–32] competes with the screening of the  $f$  shell moments due to the Kondo effect [33, 34].

The model has been applied to the equilibrium prop-

erties of a noisy quantum-dot system [35, 36] where the fluctuations of the gate voltage provide the bosonic environment. Investigating the non-equilibrium dynamics of QISs is essential for the understanding of relaxation and dissipation for these nano devices and qubits.

In the weak coupling limit, rate equations and Born-Markov approaches have been used [37, 38] to explore the real-time dynamics and the steady state. Such methods, however, cannot be employed in the strong coupling limit or close to a quantum critical point (QCP) where competing orthogonal ground states need to be accounted for. In this regime, the non-equilibrium extension of Wilson’s numerical renormalization group (NRG) approach [1, 39], the time-dependent numerical renormalization group (TD-NRG) [40, 41], has been used to access the real-time dynamics in QISs with purely fermionic or bosonic baths [40–46] or steady-state currents through nano devices [47–49]. Recently, real-time quantum Monte-Carlo approaches [50–53] and multi-layer multiconfiguration time-dependent Hartree methods [54, 55] have also been successfully applied to such problems as well as the density matrix renormalization group, see Ref. [56] for a recent review.

This paper focuses on the real-time dynamics of an Anderson impurity coupled to a bosonic as well as a fermionic bath. For that purpose, we have extended the recently introduced Bose-Fermi NRG [15] to non-equilibrium using the TD-NRG. The BFAM and the sub-ohmic spin-boson model (SBM) belong to the same universality class [15, 18, 20] for an ungaped fermionic coupling function. It has been shown that the BFAM exhibits a complicated phase diagram [15, 18, 20] for a pseudo-gap density of states (DOS) whose low-energy

properties are characterized by the exponent  $r$ :  $\rho(\varepsilon) \propto |\varepsilon|^r$ . Although  $r = 1$  is relevant for quantum impurities in  $d$  wave superconductors and charge-neutral graphene at low energies, we use  $r$  as a model parameter only in the range  $0 \leq r < 1/2$  since in this regime QPTs between a free local moment phase and a screened magnetic moment phase are found due to the Kondo effect. The low-frequency part of the bosonic bath coupling function  $J(\omega)$  can also be approximated by a power-law [57]:  $J(\omega) \propto \omega^s$ . In this paper we will focus on the sub-ohmic regime  $1/2 < s < 1$  to avoid the NRG deficiency [58–60] in the regime  $0 < s < 1/2$  and we will comment on the case of an arbitrary  $s$ .

The equilibrium properties of the BFAM [18] reveal a QPT with hyperscaling behavior for the above stated regimes for  $r$  and  $s$ . The specific combinations of the bath exponents  $r$  and  $s$  have not only a profound impact on the equilibrium properties of the QPT, but also divide different regimes in the real-time dynamics. We will show that for a final Hamiltonian, whose low-energy fixed point (FP) is mainly governed by the fermionic bath properties (F-type), the non-equilibrium dynamics of the BFAM can be exactly reproduced by a purely fermionic single-impurity Anderson model (SIAM) replacing the bare  $U$  by an  $U_{\text{ren}}$  which includes the attractive electron-electron interaction mediated by the bosonic bath.

For exponents where the low-temperature FP is governed by the bosonic bath (B-type) [20], the real-time dynamics shows distinctive differences to those in an effective SIAM defined by appropriate values of  $U_{\text{ren}}$  such that the local thermodynamic expectation values are in both models identical for the initial and final parameters of the Hamiltonian. Although, the local thermodynamic expectation values are identical the two models can be in two different low-temperature phases: While the dynamics in the BFAM is driven by the localized phase, the dynamics in effective SIAM is still governed by the strong coupling FP leading to a deviating dynamics when comparing the real-time dynamics of the same local quantities in both models.

For quenches of the gate voltage, we find different steady-state values for the impurity charge filling for identical bath couplings depending on the choice of the initial conditions since the FP of the final Hamiltonian is in the localized phase. We will demonstrate thermalization within the numerical accuracy of the method for Hamiltonians approaching the strong coupling FP. The microscopic mechanism of experimentally observed hysteretic behavior of the  $I(V)$  curves [61] in molecular junctions when sweeping the voltage with a very small but finite rate is still unsolved. It has been suggested that such a behavior might be related to conformational changes in these complex molecules [62, 63]. At infinitely large times and at finite temperatures, a real molecular junction should approach a unique steady state [49, 64]. Using a reduced density matrix formalism for the spinless version of a two-lead BFAM, Wilner *et al.* have found a bistability in the real-time evolution of the molecular

electronic occupancy [54, 55] depending on two different initial preparations of the bosonic bath configuration. The major difference between a spinless and a spinfull BFAM is the sign of the effective Coulomb interaction generated by the electron-boson interaction. In the spinless case, a repulsive interaction between the local electron density and the local conduction electrons are generated and an effective interacting resonant level model [65, 66] emerges. The effective equilibrium Coulomb repulsion  $U_{\text{ren}}$  can be extracted [49, 67] and favors coherent oscillations [68] in the real-time dynamics. In contrary, a local attractive Coulomb interaction mediated by bosons is induced [69] for models including the spin as investigated in this paper. In addition, such models exhibit quantum phase transitions for large electron-boson couplings [18, 20] and might, therefore, also contain bistabilities, depending on the initial conditions. In this paper, however, we focus on a spinfull single-lead BFAM.

## A. Plan of the paper

This paper is organized as follows: In Sec. II we present the model of interest, the Bose-Fermi Anderson model (Sec. II A), and introduce the numerical tools, the NRG (Sec. II B) and the TD-NRG (Sec. II C). To prepare the reader for the dynamics, we summarize the main equilibrium properties of the system in Sec. III. After some general remarks, where we will classify the F-type, B-type and M-type bath exponent combinations [18, 20], we will discuss the generation of an additional attractive Coulomb interaction due to the coupling to the bosonic bath in Sec. III B and provide an overview of the known phases and fixed points in Sec. III D for the ph-symmetric model. The equilibrium expectation value of the double occupancy will be used to define a mapping between the BFAM and an effective SIAM, as introduced in Sec. III E.

In Sec. IV we present our results on the non-equilibrium dynamics in the BFAM. We distinguish between F-type bath exponents in Sec. IV A, where the dynamics are reproduced exactly by an effective SIAM, and B-type bath exponents in Sec. IV B, for which distinctive differences in the dynamics between the BFAM and SIAM have been found. While in those sections ph symmetry remains maintained at any time, we focus on the influence of a sudden change of a gate voltage, breaking ph symmetry, on the dynamics of the impurity charge occupancy in Sec. IV C. We end this paper with a brief conclusion.

## II. THEORY

### A. The Bose-Fermi Anderson model

The Bose-Fermi Anderson model consists of an Anderson impurity [70] that hybridizes with conduction

band electrons and additionally couples to an ungaped fermionic bath with a continuous spectrum via its electron density. The origin of the bosons can be either acoustic phonons [21, 22] or bosonized magnetic fluctuations with the extended DMFT [18, 20]. In recent years, its equilibrium properties have been extensively studied using Wilson's NRG [18, 20].

The Hamiltonian of the charge-coupled Bose-Fermi Anderson model comprises several parts: (i) the free conduction-electron bath

$$H_F = \sum_{\vec{k}, \sigma} \epsilon_{\vec{k}} c_{\vec{k}, \sigma}^\dagger c_{\vec{k}, \sigma} \quad (1)$$

where  $c_{\vec{k}, \sigma}^\dagger$  creates a quasiparticle with the dispersion  $\epsilon_{\vec{k}}$  and spin  $\sigma$ , and non-interacting bosons

$$H_B = \sum_{\vec{q}} \omega_{\vec{q}} b_{\vec{q}}^\dagger b_{\vec{q}} \quad (2)$$

where  $b_{\vec{q}}^\dagger$  creates a bosonic excitation with the momentum  $\vec{q}$  and the dispersion  $\omega_{\vec{q}}$ , and (ii) the impurity part of a spin-degenerate impurity level

$$H_{\text{imp}} = \epsilon_d (n_{d\uparrow} + n_{d\downarrow}) + U n_{d\uparrow} n_{d\downarrow} \quad (3)$$

in the absence of a magnetic field. The operator  $d_\sigma^\dagger$  creates an impurity electron with spin  $\sigma$  and the single-particle energy  $\epsilon_d$ . The spin-dependent electron density of the impurity is represented by  $n_{d\sigma} = d_\sigma^\dagger d_\sigma$ , and  $U$  denotes the local Coulomb repulsion. (iii) The interaction between the impurity and the conduction band is given by

$$H_{\text{int}, F} = \sum_{\vec{k}, \sigma} \left( V_{\vec{k}} c_{\vec{k}, \sigma}^\dagger d_\sigma + V_{\vec{k}} d_\sigma^\dagger c_{\vec{k}, \sigma} \right) \quad (4)$$

and the local electron charge couples to each displacement of the bosonic modes

$$H_{\text{int}, B} = \left( \sum_{\sigma} n_{d\sigma} - 1 \right) \sum_{\vec{q}} g_{\vec{q}} \left( b_{\vec{q}}^\dagger + b_{\vec{q}} \right) \quad (5)$$

via the coupling constants  $g_{\vec{q}}$  and its form ensures particle-hole symmetry. The full Hamiltonian

$$H_{\text{BFAM}} = H_{\text{imp}} + H_F + H_B + H_{\text{int}, F} + H_{\text{int}, B} \quad (6)$$

determines the thermodynamics and the dynamics of the system.

### 1. Fermionic bath

In the absence of a bosonic bath the dynamics of the magnetic impurity is fully determined by the coupling function [4, 6, 7, 71]

$$\Gamma_\sigma(\varepsilon) = \pi \sum_{\vec{k}} V_{\vec{k}}^2 \delta(\varepsilon - \varepsilon_{\vec{k}, \sigma}) \quad (7)$$

which we will take as spin-independent in the following. Ignoring the spectral details of its high-energy part, which only influence the values of the relevant energy scales, but do not determine the low-energy fixed point spectrum,  $\Gamma(\varepsilon)$  is replaced by the particle-hole symmetric power-law [6, 7, 71, 72] of the form

$$\Gamma(\varepsilon) = \Gamma_0 \left| \frac{\varepsilon}{D} \right|^r \Theta(D - |\varepsilon|) \quad (8)$$

with the exponent  $r$  and the cutoff  $D$ , which defines the effective bandwidth. Note that with this definition the integral over the coupling function,

$$\pi V_0^2 = \int \Gamma(\varepsilon) d\varepsilon = \frac{2\Gamma_0 D}{r+1} \quad , \quad (9)$$

is dependent on the bath exponent  $r \geq 0$ : With increasing  $r$  the hybridization  $V_0$  decreases.

The parameter  $\Gamma_0$  serves as energy unit of the problem that turns into the standard charge fluctuation scale for a constant DOS ( $r = 0$ ). While  $r = 0$  and  $r = 1$  are the prototypical experimental realizations —  $r = 1$  is relevant in  $d$  wave superconductors or in graphene — we take  $r$  as an arbitrary parameter of the model. Furthermore, the particle-hole asymmetry is governed by the parameter  $\Delta\epsilon = 2\epsilon_d + U$ .

### 2. Bosonic bath

Decoupling the fermionic bath, the local impurity dynamics is completely determined by the bosonic bath coupling function

$$J(\omega) = \pi \sum_{\vec{q}} g_{\vec{q}}^2 \delta(\omega - \omega_{\vec{q}}) \quad (10)$$

which is approximated by the power-law form [8]

$$J(\omega) = 2\pi g \omega_c^{1-s} \omega^s \Theta(\omega_c - \omega) \quad (11)$$

for the same reason as in the fermionic case: The low-frequency properties and the nature of the quantum critical points are governed by the exponent  $s$ . The cutoff  $\omega_c$  defines the high-energy scale while the overall coupling strength is denoted by the dimensionless coupling  $g$ .

The exponent  $s$  separates different bath types:  $0 < s < 1$  for a sub-ohmic dissipation [10],  $s = 1$  for ohmic dissipation [8] and  $s > 1$  for a super-ohmic bath [73]. In the following we restrict ourselves to bosonic exponents  $1/2 \leq s \leq 1$  due to so far unresolved problems applying the NRG [59] for the sub-ohmic spin-boson model with  $0 < s < 1/2$ .

## B. The numerical renormalization group for Bose-Fermi systems

The numerical renormalization group (NRG) is well established for fermionic systems [3–5]. In the last decade

the NRG has been extended to bosonic environments [9, 10, 60, 74, 75] and lately combined for Bose-Fermi impurity systems [14, 15, 18]. We shortly summarize the NRG procedure [15] for an environment consisting of bosonic as well as fermionic DOFs.

The bath continua of the two baths will be *discretized logarithmically* with the discretization parameter  $\Lambda > 1$  [3]. The fermionic conduction band is divided into the intervals  $[\Lambda^{-(n+1)}D, \Lambda^{-n}D]$  and  $[-\Lambda^{-n}D, -\Lambda^{-(n+1)}D]$  regarding the bandwidth  $D$  and covers positive and negative energies. The bosonic bath is divided into the intervals  $[\Lambda^{-(m+1)}\omega_c, \Lambda^{-m}\omega_c]$  regarding the high-energy cut-off  $\omega_c$  and covers only positive energies. The indexes  $n, m = 0, 1, 2, \dots$  enumerate the fermionic and bosonic intervals. In each interval only one discrete energy is used as representative, which is the main approximation of the NRG [1, 3]. For simplicity we set both bath cut-offs equal:  $D/\omega_c = 1$ .

This assumption introduced by Glossop *et al.* [15] is well justified when targeting the low-energy physics and quantum phase transitions. One could start with  $D_0 \gg D$  and apply an RG procedure to the problem until the effective bandwidth  $D_{\text{eff}} \approx \omega_c$  is reached. This would give rise to an effective impurity model with renormalized parameters  $\epsilon_{d,\text{eff}}$  and  $U_{\text{eff}}$  as well as slightly modified  $\Gamma_{\text{eff}}(\omega)$  entering Eq. (7).

The discretized bath Hamiltonians can be exactly transformed via a Householder transformation onto two semi-infinite Wilson chains, the fermionic bath

$$\frac{H_F}{D} = \sum_{\sigma, n=0}^{\infty} \left( \epsilon_n f_{\sigma, n}^\dagger f_{\sigma, n} + \tau_n \left( f_{\sigma, n}^\dagger f_{\sigma, n+1} + h.c. \right) \right) \quad (12)$$

and the bosonic bath

$$\frac{H_B}{\omega_c} = \sum_{m=0}^{\infty} \left( \omega_m b_m^\dagger b_m + t_m \left( b_m^\dagger b_{m+1} + h.c. \right) \right). \quad (13)$$

By this procedure, the impurity couples only to the first chain link of the fermionic and the bosonic chain, as it is depicted in Fig. 1 and  $H_0$  is given by

$$H_0 = \epsilon_d (n_{d\uparrow} + n_{d\downarrow}) + U n_{d\uparrow} n_{d\downarrow} + V_0 \sum_{\sigma} \left( f_{0\sigma}^\dagger d_{\sigma} + d_{\sigma}^\dagger f_{0\sigma} \right) + g_0 (n_d - 1) (b_0^\dagger + b_0) \quad (14)$$

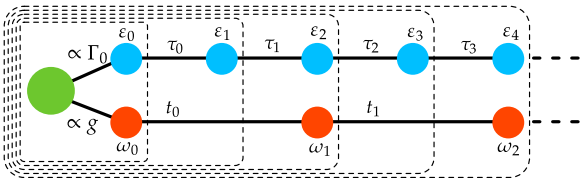


FIG. 1. (Color online) Sketch of the discretized model. The impurity (green) only couples to the first sites of the two independent Wilson chains representing the bosonic (red) and fermionic (blue) bath. The dashed boxes indicate the subsystems after each NRG iteration starting with the innermost one. Adapted from [15].

with  $g_0 = \omega_c \sqrt{2g/(s+1)}$  [18].

Since the fermionic bath contains positive and negative energies, whereas the bosonic bath only contains positive energies, the fermionic Wilson chain parameters scale as  $\epsilon_n, \tau_n \propto \Lambda^{-n/2}$ , while the bosonic Wilson chain parameters scale as  $\omega_m, t_m \propto \Lambda^{-m}$ . In order to maintain the correct energy hierarchy in both types of baths, we need to add a bosonic site only every other NRG iteration as indicated by the dashed boxes in Fig. 1.

The Hilbert space of the bosonic operators  $b_m$  has to be restricted within the numerics to a finite size. Here, we will use the standard harmonic oscillator eigenbasis, i.e.  $b_m^\dagger b_m |n_m\rangle = n_m |n_m\rangle$ , with  $n_m = 0, \dots, N_B$  excitations. The enlarged Hamiltonian is diagonalized by exact diagonalization. By adding one chain link (or two at each odd iteration) the Hilbert space of the Hamiltonian grows exponentially with  $n$  ( $m$ ). Therefore, we have to truncate the Hilbert space and keep only the  $N_S$  eigenstates of the Hamiltonian with the lowest many-body energies.

The renormalization group transformation  $R$ ,  $H_{n+1} = R(H_n)$ , approaches a scale-invariant low-energy fixed point (FP) for large  $n$ . As for models with only fermionic baths [3], the FP is connected to the transformation  $R^2$ , not  $R$  as for bosonic baths, due to the different ground state spin configurations for chains with even and odd numbers of sites [15].

### C. The time-dependent numerical renormalization group

We use the time-dependent numerical renormalization group (TD-NRG) [40, 41] to calculate the time evolution of local impurity quantities after a sudden quench:  $H(t) = H_i \Theta(-t) + H_f \Theta(t)$ .

Due to the exponential growth of the Hilbert space, high-energy states are discarded after each iteration. Since the initial basis set is known, the set of all discarded states forms a complete basis set and simultaneously serves as an approximate eigenbasis of the Hamiltonian governing the time evolution of the problem.

Then, the time-dependent expectation value  $\langle O(t) \rangle$  of a general local operator  $\hat{O}$  can be casted into the form

$$\langle O(t) \rangle = \sum_n \sum_{r,s}^{\text{trun}} e^{it(E_r^n - E_s^n)} O_{r,s}^n \rho_{s,r}^{\text{red}}(n) \quad (15)$$

where  $E_r^n$  and  $E_s^n$  are the dimension-full NRG eigenenergies of the Hamiltonian  $H_f = H(t > 0)$  at iteration  $n \leq N$  and  $O_{r,s}^n$  is the matrix representation of  $\hat{O}$  at that iteration.  $\rho_{s,r}^{\text{red}}(n)$  is the reduced density matrix defined as

$$\rho_{s,r}^{\text{red}}(n) = \sum_e \langle s, e; n | \hat{\rho}_0 | r, e; n \rangle \quad (16)$$

where  $\hat{\rho}_0$  is the initial density operator of the problem prior to the quench. The restricted sum over  $r$  and  $s$

in Eq. (15) requires that at least one of these states is discarded at iteration  $n$ .

Implementing the TD-NRG requires two NRG runs: one for the initial Hamiltonian  $H_i = H(t < 0)$  to construct the initial density operator  $\hat{\rho}_0$  of the system and one for  $H_f$  to obtain the approximate eigenbasis governing the time evolution in Eq. (15). For more details on the TD-NRG see Refs. [40, 41]. Recently, the TD-NRG has been extended to use the full density matrix including pulsed Hamiltonians [44] and periodic switching [76]. Also a hybrid approach [77] with TD-NRG and DMRG extended the scope of application.

In the original implementation of the TD-NRG [41] each phase factor in Eq. (15)

$$e^{it(E_r^n - E_s^n)} \rightarrow e^{it(E_r^n - E_s^n) - \Gamma_n t} \quad (17)$$

has been supplemented with an energy-resolution dependent damping factor  $\Gamma_n = \alpha \varepsilon_n$  proportional to the energy scale  $\varepsilon_n = D\Lambda^{-(n-1)/2}(1 + 1/\Lambda)/2$  at iteration  $n$  for all  $E_r^n - E_s^n \neq 0$ , and  $\alpha = O(1)$ . It mimics an additional decay due to the continuum of modes neglected by the NRG discretization that is also used for the broadening of the NRG Lehmann representation of equilibrium spectral functions [1, 78, 79].

However, since such an artificial broadening [78] lacks the detailed information about additional physical decay processes not included in the NRG Hamiltonian, it could lead to wrongly damp out oscillatory contributions at long times. In order to avoid any prejudice, we usually set  $\alpha = 0$  and use instead the  $z$  averaging [80] to minimize discretization-related oscillations.

### III. EQUILIBRIUM PROPERTIES

#### A. General remarks

To set the stage for our investigation of the real-time dynamics of the BFAM in the vicinity to quantum phase transitions, we begin with a summary of the main equilibrium properties and present the phase diagram of the BFAM in the parameter space spanned by  $U/\Gamma_0$  and  $g$ .

The equilibrium properties of the BFAM are well understood by several publications [6, 7, 17, 18, 20, 81–85]. Due to the richness of the phase diagram of the BFAM we give an overview of the different NRG fixed points (FPs) and explain by which quantities we classify the phases.

Within this paper, we focus on a particle-hole (ph) symmetric final Hamiltonian  $H_f$ , i.e.  $U_f = -2\epsilon_{d,f}$ . We will investigate two classes of quenches: (i)  $H_i$  also obeys ph symmetry and (ii)  $H_i$  describes an initially ph symmetry broken phase.

In the first case, the level occupancy is  $\langle n_d(t) \rangle = 1$  for all times, and there are two pairs of locally degenerated states: the empty- and the double-occupied state  $|0\rangle, |2\rangle$  and, in absence of an external magnetic field the two spin states  $|\sigma\rangle$  which contain exactly one electron.

Depending on the combination matrix  $(r, s)$  three types of quantum critical regimes have been identified in the model, see Fig. 13 in Ref. [20]. For small  $r$ , the bosonic bath properties govern the critical exponents of the thermodynamic properties defining a B-type regime with a boundary  $0.5 \leq s = 1 - 2r \leq 1$ . For larger  $r$  and  $s$  the critical exponents are given by the fermionic bath properties, hence defining the F-type regime with a non-linear boundary. Between the two regimes there is a mixed (M) type regime where the exponents do not decompose in fermionic and bosonic parts.

Firstly, we show below, that the real-time dynamics in the F-type regime can essentially be reproduced by a pseudo-gap SIAM with a renormalized  $U_{\text{ren}}$  while the non-equilibrium dynamics in the B-type regime differs from those of an effective SIAM and are affected by an additional damping provided by the relevant bosonic modes present in the fixed point spectrum.

Secondly, starting from an initially ph symmetry broken state, we track the real-time dynamics of the level occupancy  $\langle n_d(t) \rangle$ , but restrict ourselves to  $r = 0$ . A thorough discussion of the corresponding equilibrium properties of the asymmetric model can be found in Refs. [18, 20] and are only relevant for the initial preparation of the system and entering  $\rho_0$ .

For the calculations of the BFAM we use  $U/\Gamma_0 = 1$ ,  $\Gamma_0/D = 0.01$  and vary over the bosonic coupling  $g$ . For the comparison with the SIAM, we also use  $\Gamma_0/D = 0.01$  but vary over  $U/\Gamma_0$  with the same fermionic bath exponent  $r$ . All our (TD-)NRG calculations are done with  $\Lambda = 6$ , and  $N = 40$  NRG iterations. For the BFAM we use  $N_S = 1000$ ,  $N_B = 10$ , while for the SIAM we keep instead  $N_S = 2000$  states at each iteration. We average over  $N_z = 8$  different bath realizations. For the equilibrium results we forgo sometimes this averaging (no  $z$  averaging) to minimize the numerical effort. Therefore, the numerical values of the critical couplings depend on whether or not the  $z$  averaging has been done.

#### B. Renormalization of the Coulomb repulsion

In order to understand qualitatively the major features of the phase diagram and construct an effective SIAM, we briefly review the boson-mediated attractive electron-electron interaction. To keep it simple, we consider a decoupled fermionic bath by setting  $\Gamma_0 = 0$ . Then, the remaining Hamiltonian reads

$$H' = \epsilon_d (n_{d\uparrow} + n_{d\downarrow}) + U n_{d\uparrow} n_{d\downarrow} + \sum_{\vec{q}} \omega_{\vec{q}} b_{\vec{q}}^\dagger b_{\vec{q}} + (n_d - 1) \sum_{\vec{q}} g_{\vec{q}} \left( b_{\vec{q}}^\dagger + b_{\vec{q}} \right) \quad (18)$$

Since the number of fermions is conserved,  $H'$  can be diagonalized in each particle number subspace separately. For  $|\sigma\rangle$  the fermion-boson interaction vanishes and the bath decouples. The two other states,  $|0\rangle$  and  $|2\rangle$ , require

displaced harmonic oscillator operators  $\tilde{b}_{\vec{q}} = b_{\vec{q}} + \theta_{\vec{q}}$  and the effective bath Hamiltonian is given by [18]

$$\langle 0|H|0\rangle = \sum_{\vec{q}} \omega_{\vec{q}} \tilde{b}_{\vec{q}}^\dagger \tilde{b}_{\vec{q}} - \sum_{\vec{q}} \frac{g_{\vec{q}}^2}{\omega_{\vec{q}}} \quad \text{and} \quad (19)$$

$$\begin{aligned} \langle \uparrow\downarrow|H|\uparrow\downarrow\rangle &= 2\epsilon_d + U + \sum_{\vec{q}} \omega_{\vec{q}} \tilde{b}_{\vec{q}}^\dagger \tilde{b}_{\vec{q}} - \sum_{\vec{q}} \frac{g_{\vec{q}}^2}{\omega_{\vec{q}}} \\ &= 2\epsilon_d + U_{\text{ren}} + \sum_{\vec{q}} \omega_{\vec{q}} \tilde{b}_{\vec{q}}^\dagger \tilde{b}_{\vec{q}} \end{aligned} \quad (20)$$

with the displacements  $\theta_{\vec{q}} = \pm g_{\vec{q}}/\omega_{\vec{q}}$  and the renormalized Coulomb repulsion

$$U_{\text{ren}} = U - \sum_{\vec{q}} \frac{g_{\vec{q}}^2}{\omega_{\vec{q}}} = U - g \frac{2\omega_c}{s} \quad (21)$$

using the bosonic coupling function defined in Eqs. (10) and (11).

This effective Coulomb repulsion changes sign and becomes attractive for  $g > Us/(2\omega_c)$ . The sign change causes a level crossing between the two degenerated magnetic states  $|\sigma\rangle$  and the degenerated charge states  $|0\rangle, |2\rangle$  for ph-symmetric parameters. At  $g' = Us/(2\omega_c)$  the renormalized Coulomb repulsion vanishes:  $U_{\text{ren}}(g') = 0$ .

### C. Definition of the effective spin and charge moments

The effective local moment [39]

$$\mu_{\text{eff}}^2(T) = \Delta \left( \langle S_z^2(T) \rangle - \langle S_z(T) \rangle^2 \right) \quad (22)$$

can be used to identify the quantum critical point (QCP).  $\Delta(X)$  measures the macroscopic observable  $X$  in presence of the impurity and the Wilson chain and subtracts the effect of the quantity  $X$  of the pure Wilson chain without the impurity at temperature  $T$ , and  $S_z$  denotes the z component of the total spin of the system.

In the continuum  $\langle X \rangle, \langle X^2 \rangle$  are extensive and diverge with the system size. By the definition of  $\Delta(X)$  [3, 7] the impurity contribution of the quantity  $X$  is extracted, which is of the order  $O(1)$ . Note, however, that  $\mu_{\text{eff}}^2(T)$  does not measure the local impurity spin observable but rather the difference in the total system properties with and without the impurity. Hence, the effective impurity spin moment  $\mu_{\text{eff}}^2(T)$  is in general related to a degree of freedom (DOF) comprising a linear combination of local and conduction electron spin observables.

Analog to  $\mu_{\text{eff}}^2(T)$ , we can define an effective charge moment

$$Q_{\text{eff}}^2(T) = \frac{1}{4} \Delta \left( \langle Q^2(T) \rangle - \langle Q(T) \rangle^2 \right) \quad (23)$$

whereby  $Q$  is the total charge of the system with respect to half-filling.

### D. Overview of the phases

Ignoring the details of the F-, B- and M-type regimes, three stable FPs are found for the ph-symmetric BFAM for  $r > 0$ ,  $1/2 < s < 1$  and a finite  $U > U_c$ .

Starting with  $g = 0$  in the local moment (LM) FP, an effective spin  $S = 1/2$  DOF decouples from the problem as it is indicated by  $\lim_{T \rightarrow 0} \mu_{\text{eff}}^2(T) = 1/4$  and  $\lim_{T \rightarrow 0} Q_{\text{eff}}^2(T) = 0$ .

Increasing  $g$  reduces  $U_{\text{ren}}$  such that the effective Kondo interaction exceeds the critical value: In the Kondo-screened symmetric strong coupling (SSC) FP the impurity spin is partially screened with  $\lim_{T \rightarrow 0} \mu_{\text{eff}}^2(T) = r/8$  and simultaneously  $\lim_{T \rightarrow 0} Q_{\text{eff}}^2(T) = r/8$ . This universality of the effective moments indicates that the conventional spin Kondo effect and the charge Kondo effect are adiabatically connected and can only be separated by their crossover behavior: There exists only one universal FP in the ph-symmetric regime. In the spin Kondo regime,  $\mu_{\text{eff}}^2(T)$  approaches the value  $r/8$  from above and  $Q_{\text{eff}}^2(T)$  from below when lowering the temperature, as seen in Fig. 2. In the charge Kondo regime the role of  $Q_{\text{eff}}^2(T)$  and  $\mu_{\text{eff}}^2(T)$  is interchanged. The transition from the LM to the SSC FP occurs at  $g = g^*$  and is governed by an unstable FP.

Once  $g$  exceeds  $g_c > g^*$  with  $U_{\text{ren}} < 0$ , we reach the localized (L) FP characterized by a free charge moment, i.e.  $\lim_{T \rightarrow 0} Q_{\text{eff}}^2(T) = 1/4$  and  $\lim_{T \rightarrow 0} \mu_{\text{eff}}^2(T) = 0$ . Since

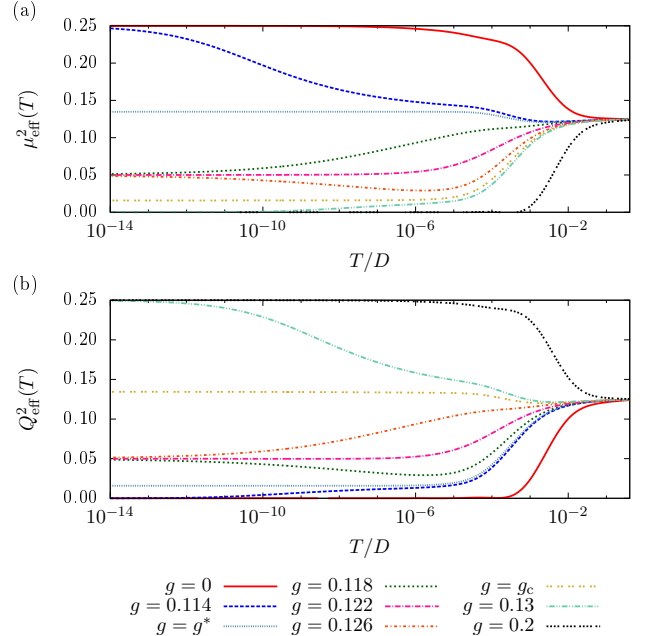


FIG. 2. (Color online) Effective moments (a)  $\mu_{\text{eff}}^2(T)$  and (b)  $Q_{\text{eff}}^2(T)$  for bath exponents  $(r, s) = (0.4, 0.8)$  without  $z$  averaging. The BFAM parameters are  $\Gamma_0/D = 0.01$  with the ratio  $U/\Gamma_0 = 1$ . Different FPs are reached for  $T \rightarrow 0$ . The unstable critical FPs have the couplings  $g^* = 0.11496(5)$  and  $g_c = 0.12847(7)$ .

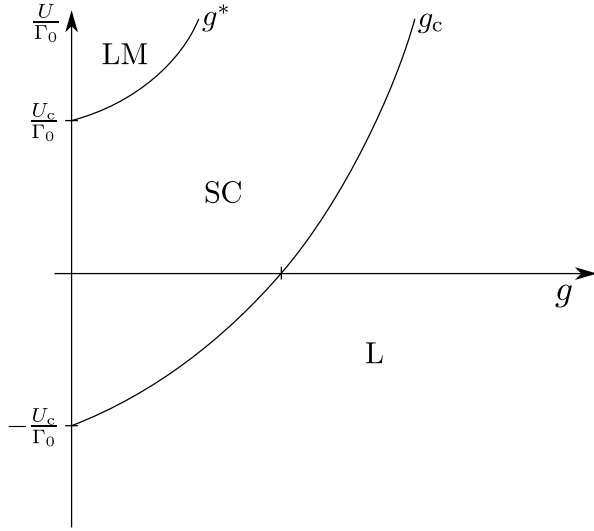


FIG. 3. Sketch of the phase diagram of the BFAM in dependence of the ratio  $U/\Gamma_0$  and the bosonic coupling  $g$ . The bosonic bath exponent is sub-ohmic  $1/2 < s < 1$  and the fermionic exponent is  $0 < r < 1/2$ . The critical  $U_c/\Gamma_0$  is already known for the SIAM. The phase boundaries  $g^*$  and  $g_c$  separate the local moment (LM), the symmetric strong coupling (SSC) and the localized (L) phase, respectively.

a free charge moment decouples from the continuum and the spin momentum vanishes, this FP mirrors the LM FP where  $U_{\text{ren}} > 0$ .

The two QCPs at  $g = g_c$  and  $g = g^*$ , governing the transition between the LM FP and the SSC FP ( $g^*$ ) and the transition between the SSC FP and the L FP ( $g_c$ ), are characterized by two unstable FPs with  $Q_{\text{eff}}^2(T \rightarrow 0, g_c) = \mu_{\text{eff}}^2(T \rightarrow 0, g^*)$  and  $Q_{\text{eff}}^2(T \rightarrow 0, g^*) = \mu_{\text{eff}}^2(T \rightarrow 0, g_c)$ .

This series of FPs can be reached by a single parameter scan as long as  $U > U_c$  for  $g = 0$ .  $U_c$  separates the LM FP and an SSC FP in the pg SIAM in the absence of a bosonic bath [6, 7]. For  $0 < U < U_c$ , the LM FP is absent and only the SSC FP remains for  $g = 0$ .

We illustrate the approach of the different FPs for a F-type exponent combination  $(r, s) = (0.4, 0.8)$  and  $U/\Gamma_0 = 1$ ,  $\Gamma_0/D = 0.01$  in Fig. 2.  $\mu_{\text{eff}}^2(T)$  is depicted in Fig. 2(a) and  $Q_{\text{eff}}^2(T)$  is shown in Fig. 2(b) for the same set of bosonic couplings  $g$ . All 5 FP values (3 stable, 2 unstable) emerge in the zero-temperature limit by varying over the bosonic coupling  $g$ .

We complete our overview with the generic phase diagram for  $0 < r < 1/2$  and  $1/2 < s < 1$  shown in Fig. 3 where we have extended the previous investigations [18, 20] to negative  $U$ . The phase boundaries  $(U, g^*)$  and  $(U, g_c)$  start at the well-known phase boundary points of the SIAM [6, 85]:  $U_c/\Gamma_0$  separates the LM and the SSC phases and  $-U_c/\Gamma_0$  separates the SSC and L phases. For infinitely large  $U/\Gamma_0$  both phase boundaries  $g^*$  and  $g_c$  merge.

It contains an important message: The three stable

FPs can either be reached for fixed  $U > U_c$  by tuning  $g$  or for a fixed  $g$  by tuning  $U$ . As discussed in Sec. III B above, the leading order effect of the bosonic bath coupling is the reduction of  $U$  to a renormalized value which is given by Eq. (21) in the absence of the fermionic bath.

### E. Equilibrium double occupancy

Now we turn to the equilibrium double occupancy  $\langle D \rangle_{\text{eq}}$  for different bath exponent combinations  $(r, s)$ . While  $\mu_{\text{eff}}^2(T \rightarrow 0)$  and  $Q_{\text{eff}}^2(T \rightarrow 0)$  jump at and across the QCP,  $\langle D \rangle_{\text{eq}}$  varies continuously [7, 46] as function of  $g$  as demonstrated in Fig. 4 for  $U/\Gamma_0 = 1$  and  $\Gamma_0/D = 0.01$ .

Although the estimate in Eq. (21) for  $U_{\text{ren}}$  does not hold at finite  $\Gamma_0$ , we can generalize the definition of  $g'$ :

$$\langle D \rangle_{\text{eq}}(g') = 1/4 \quad . \quad (24)$$

At this value the occupation probability of all four local states are equal corresponding to  $U = 0$  for  $g = 0$  and the value is indicated by the solid horizontal line in Fig. 4. As discussed above,  $g'$  can be viewed as the crossover parameter from the spin Kondo to the charge Kondo regime in the interval  $g^* < g' < g_c$ . Since  $U_{\text{ren}}$  is essentially governed by the bosonic bath, all curves in Fig. 4(b) cross each other in one point,  $\langle D \rangle_{\text{eq}} = 1/4$ , revealing that  $U_{\text{ren}}(g, s) = 0$  is independent of  $r$ .

Since the three stable phases of the BFAM can be reached for  $g = 0$  as well by tuning  $U$ , the question arises

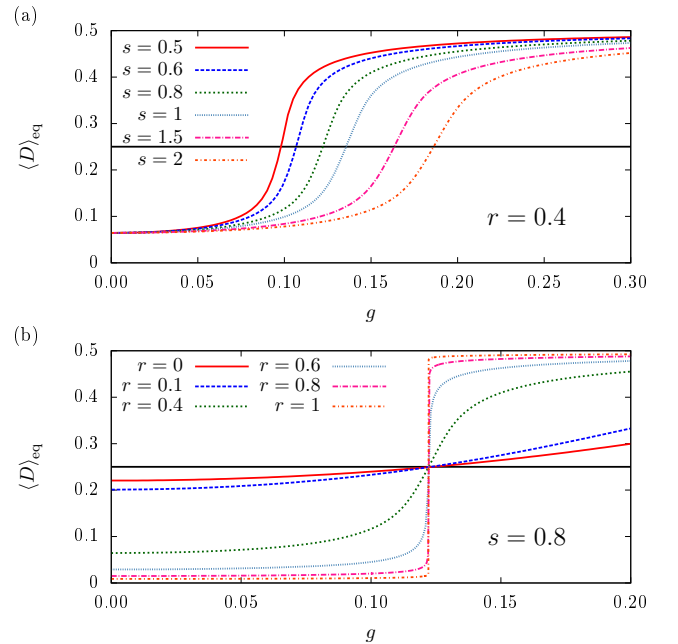


FIG. 4. (Color online) Equilibrium double occupancy  $\langle D \rangle_{\text{eq}}$  of the BFAM versus the bosonic coupling  $g$  for the fixed ratio  $U/\Gamma_0 = 1$ ,  $\Gamma_0/D = 0.01$  and without  $z$  averaging. All data is obtained in the limit  $T \rightarrow 0$ . Varying (a) over  $s$  for fixed  $r = 0.4$  and (b) over  $r$  for fixed  $s = 0.8$ .



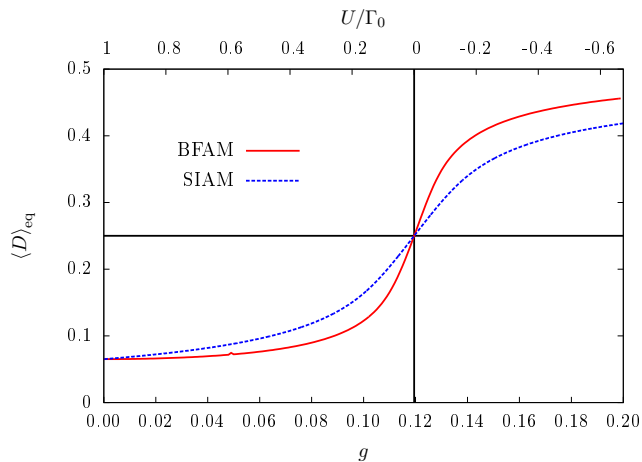


FIG. 5. (Color online) Equilibrium double occupancy  $\langle D \rangle_{\text{eq}}$  of the BFAM versus the bosonic coupling  $g$  for the fixed ratio  $U/\Gamma_0 = 1$ ,  $\Gamma_0/D = 0.01$ ,  $(r, s) = (0.4, 0.8)$  and of the SIAM versus the Coulomb interaction  $U/\Gamma_0$  for fixed  $\Gamma_0/D = 0.01$  and  $r = 0.4$ . All data is obtained in the limit  $T \rightarrow 0$  and averaged over  $N_z = 8$  realizations.

what is the influence of the additional bosonic bath beyond a renormalization  $U \rightarrow U_{\text{ren}}(g)$  on the real-time dynamics compared to the SIAM.  $\langle D \rangle_{\text{eq}}$  monotonically increases with increasing  $g$  in the BFAM and decreases with increasing  $U$  in the SIAM, as seen in Fig. 5. By the requirement

$$\langle D \rangle_{\text{eq}}^{\text{BFAM}}(g) = \langle D \rangle_{\text{eq}}^{\text{SIAM}}(U/\Gamma_0) \quad (25)$$

we define an effective SIAM that leads to the same local fermionic equilibrium expectation values for the same  $r$ .

#### IV. REAL-TIME DYNAMICS FOR THE SYMMETRIC MODEL

##### A. F-type bath exponents

As an example for the generic real-time dynamics in the BFAM we present quenches for fixed  $U/\Gamma_0 = 1$ ,  $\Gamma_0/D = 0.01$ ,  $(r, s) = (0.4, 0.8)$  by a sudden change of the coupling constant  $g$  from its initial value  $g_i$  to the final value  $g_f =: g$ .

We have picked three representative initial values: (i)  $g_i = 0$  starting from the LM FP, (ii)  $g^* < g_i = 0.119488 < g_c$  corresponding to  $\langle D \rangle_{\text{eq}}(g_i) = 1/4$  ( $U_{\text{ren}} = 0$ ) starting from the SSC FP, and (iii)  $g_c < g_i = 0.2$  deep in the L regime. For  $g_f =: g$  we select a series of values within each phase.

We will show that for the F-type bath exponents the real-time dynamics can be fully understood by mapping the BFAM onto an effective SIAM defined by Eq. (25). The corresponding values of  $U/\Gamma_0$  for the given  $g$  can be found in Tab. I. Hence, the quenches in  $g$  within the

TABLE I. Correspondence between the bosonic coupling  $g$  of the BFAM with fixed ratio  $U/\Gamma_0 = 1$ ,  $\Gamma_0/D = 0.01$ ,  $(r, s) = (0.4, 0.8)$  and the Coulomb interaction  $U/\Gamma_0$  of the SIAM defined via Eq. (25). All data is obtained in the limit  $T \rightarrow 0$ .

Phase	$\langle D \rangle_{\text{eq}}$	$g$	$U/\Gamma_0$
<b>LM</b>	<b>0.065119</b>	<b>0</b>	<b>1</b>
	0.069507	0.04	0.8917
	0.076314	0.06	0.7557
	0.089795	0.08	<b>0.5628</b>
	0.122573	0.1	0.3098
<b>SSC</b>	0.195940	0.114	0.09381
	0.214397	0.116	0.06031
	0.234426	0.118	0.02601
	<b>0.250000</b>	<b>0.119488</b>	<b>0</b>
	0.276720	0.122	-0.0449
	0.297465	0.124	-0.0816
	0.316741	0.126	-0.1188
<b>L</b>	0.392307	0.14	-0.3999
	0.428959	0.16	-0.8580
	0.446127	0.18	-1.3860
	<b>0.456499</b>	<b>0.2</b>	<b>-1.9872</b>

BFAM are mapped onto the corresponding  $U$  quenches in the SIAM.

##### 1. Quenches within a phase

In Fig. 6 we present the quenches within each of the three stable phases. We supplement the dynamics of the BFAM with those of the effective SIAM plotted in gray (color online) in the background. For all those quenches we find equilibration and the dynamics of the BFAM agrees with the effective SIAM within the numerical accuracy of the TD-NRG.

The quenches within the L phase are shown in Fig. 6(a) where we start with a large negative  $U_{\text{ren}}$  ( $g_i = 0.2$ ) and  $\langle D(t=0) \rangle$  close to  $1/2$ . A sudden reduction of  $g$  results in a reduction of the double occupancy. The double occupancy  $\langle D(t) \rangle$  smoothly declines on a timescale roughly given by  $1/\Gamma_0$  with some small  $g$ -dependent corrections.

Fig. 6(b) depicts the data for quenches starting from the degeneracy point of all local states ( $U_{\text{ren}} = 0$ ) using  $g_i = 0.119488$ . For  $g > g_i$ ,  $\langle D(t) \rangle$  increases, while for  $g < g_i$ ,  $\langle D(t) \rangle$  decreases with time. The corresponding thermal expectation values, indicated as arrows in the figure, demonstrate thermalization in the long-time limit.

Starting from a decoupled bosonic bath ( $g_i = 0$ ), quenches within the LM phase are shown in Fig. 6(c). Similar to Fig. 6(a) the equilibrated value of  $\langle D \rangle$  deviates from the thermodynamic equilibrium: the larger  $|g_f - g_i|$  the larger the deviation. This expected behavior is related to the decoupling of a charge DOF from the bath continuum in the L FP. Note, however, that the deviations are very small.

In addition, we have investigated the same type of



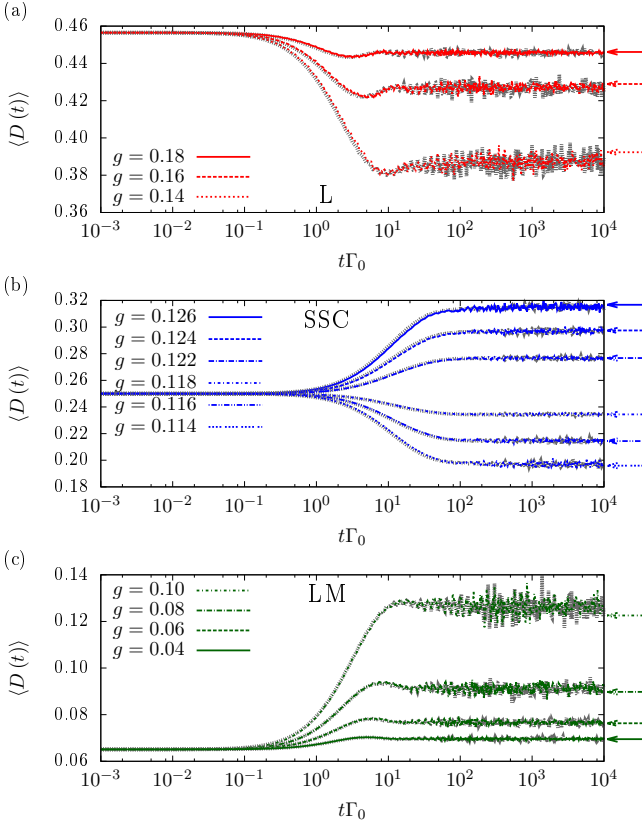


FIG. 6. (Color online) Real-time dynamics of the double occupancy  $\langle D(t) \rangle$  (colored curves) in the BFAM for bath exponents  $(r, s) = (0.4, 0.8)$  with  $U/\Gamma_0 = 1$  and  $\Gamma_0/D = 0.01$ . Gray curves in the background are the effective dynamics of the double occupancy in the SIAM. We perform quenches within the (a) L phase, (b) SSC phase and (c) LM phase. Details on the chosen couplings  $g_i$  and  $g$  are given in the beginning of Sec. IV A as well as in Tab. I.

quenches using an effective SIAM, by setting  $g_i = g_f = 0$  and switching between the corresponding  $U$  values that lead to identical  $\langle D \rangle_{\text{eq}}$ . The real-time dynamics of  $\langle D(t) \rangle$  has been added as gray curves to the graphs of Fig. 6. For all investigated cases, the effective SIAM results agree perfectly with those of the BFAM demonstrating that the effect of the bosonic bath for F-type bath exponents is fully determined by  $U_{\text{ren}}$  and the fermionic bath exponent  $r$ .

In order to extract the relevant crossover time scale  $t_{\text{co}}$ , we introduce the scaling function [41, 46]

$$f(t) = \frac{\langle D(t) \rangle - \langle D(\infty) \rangle}{\langle D(0) \rangle - \langle D(\infty) \rangle} \quad (26)$$

of the time-dependent double occupancy  $\langle D(t) \rangle$ . The function maps the dynamics onto  $f(0) = 1$  and approaches  $f(\infty) = 0$  at infinitely long times independent of the parameters. We define the crossover time scale  $t_{\text{co}}$  by demanding  $f(t_{\text{co}}) = 1/2$  and plot  $f(t)$  versus  $t/t_{\text{co}}$  in Fig. 7(a) using the data of Fig. 6. Universality of the quenches in the SSC phase (blue curves) is clearly visible.

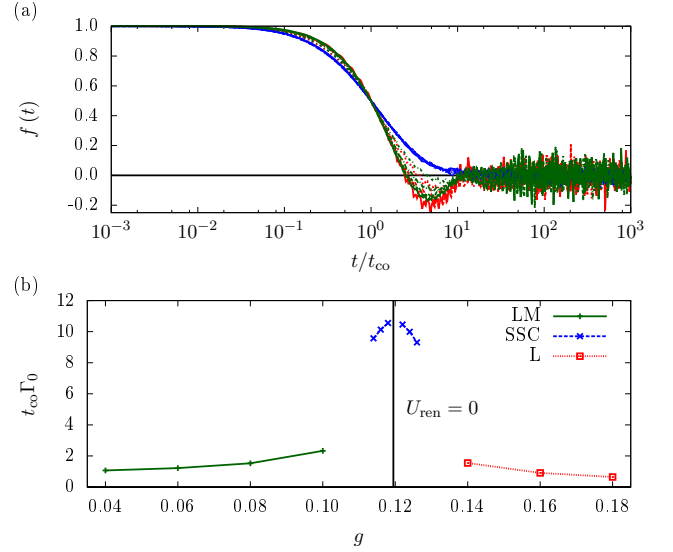


FIG. 7. (Color online) (a) Scaled dynamics of all BFAM quenches in Fig. 6 according to Eq. (26) versus the crossover time scale  $t_{\text{co}}$ . (b) Crossover time scale  $t_{\text{co}}$  versus  $g$ .

For the L phase and the LM phase comparable shapes of  $f(t/t_{\text{co}})$  are found, which slightly differ from the SSC case and are non-universal for  $t > t_{\text{co}}$ .

The extracted  $t_{\text{co}}$  versus  $g$  is shown in Fig. 7(b) for the three different phases. The vertical line marks the coupling  $\langle D \rangle_{\text{eq}}(g' = 0.119488) = 1/4$  corresponding to  $U_{\text{ren}} = 0$ . The crossover time scale shows an ascending slope for  $U_{\text{ren}} \rightarrow 0^+$  and a descending slope for an increasing attractive  $U_{\text{ren}} \rightarrow -\infty$  independent of the quench type. For the quenches using small values of  $U$  as reported in Ref. [46], the variation of  $t_{\text{co}}$  is of order of 3% which we had attributed to numerical errors at that time. Therefore, we have claimed in Ref. [46] that  $t_{\text{co}}$  remains independent of  $U$ . Our present study [86], however, suggests a dependence  $t_{\text{co}}(U_{\text{ren}})$  as depicted in Fig. 7(b).

## 2. Quenches from the SSC FP

In this section, we focus on quenches from the SSC FP with  $\langle D(g_i = 0.119488) \rangle = 1/4$  into the L and LM phase. We have found damped oscillations for both cases which equilibrate to a steady-state values significantly deviating from the thermodynamic equilibrium as shown in Fig. 8(a). The arrows at the right side of Fig. 8(a) illustrate the equilibrium double occupancy calculated by an independent NRG calculation for the final conditions. The oscillation frequency depends on the renormalized Coulomb repulsion  $|U_{\text{ren}}|$  whose values can be estimated from the effective SIAM as listed in Tab. I.

The stronger  $g$  deviates from the critical coupling  $g^*$  and  $g_c$  respectively, the more the effective local charge or spin moments are localized and contribute to  $\langle D(t) \rangle$ : the damping is reduced leading to more pronounced oscillations.

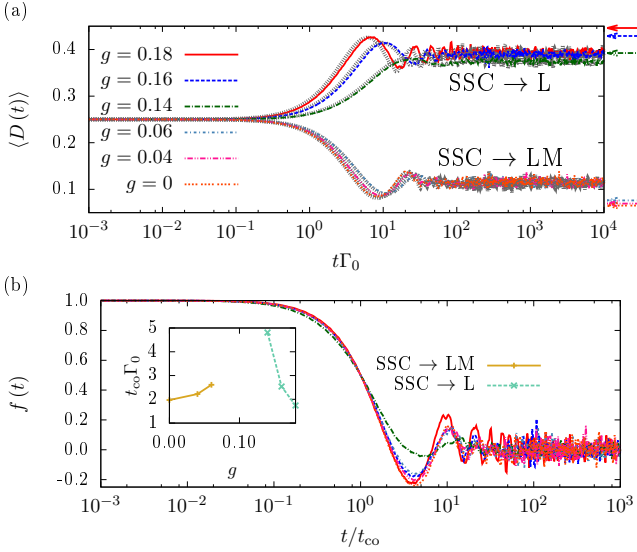


FIG. 8. (Color online) Real-time dynamics of the double occupancy  $\langle D(t) \rangle$  (colored curves) in the BFAM with the same parameters as in Fig. 6. Gray curves in the background show the corresponding double occupancy in the SIAM. (a) Quenches with the initial condition  $g_i = 0.119488$  (SSC FP) into the L and LM phase. (b) Scaled data of BFAM quenches of (a) via Eq. (26) versus the time scale  $t_{co}$ , which is depicted in the inset.

tions.

We have extracted the crossover time scale  $t_{co}$  by plotting  $f(t)$  using the data of Fig. 8(a) in Fig. 8(b) as function of  $t/t_{co}$ . Now, the locations of the oscillatory maxima and minima agree very well. The inset of Fig. 8(b) shows the dependency of  $t_{co}$  on  $g$  translating to  $t_{co} \approx 2/|U_{ren}|$ .

### 3. Quenches into the SSC phase

Now we reverse the quench direction compared to the previous section: We start from the LM or L FP and quench into the SSC phase. For both quench types the double occupancy  $\langle D(t) \rangle$  equilibrates onto a steady-state value via a smooth crossover as demonstrated in Fig. 9.

However, the steady-state values for the same  $H_f$  are slightly different: The value for a quench starting from the L FP always exceeds the value for the quench starting from the LM FP. Nevertheless, the deviation from the equilibrium NRG value remains very small as indicated by arrows on the right side of Fig. 9(a) and is related to the TD-NRG discretization errors. Therefore, we conclude that the quenches into the SSC phase thermalize in the continuum limit.

Fig. 9(b) reveals perfect universality of the function  $f(t/t_{co})$ . This illustrates that the quenches from the L or LM FP are mirror images of each other.

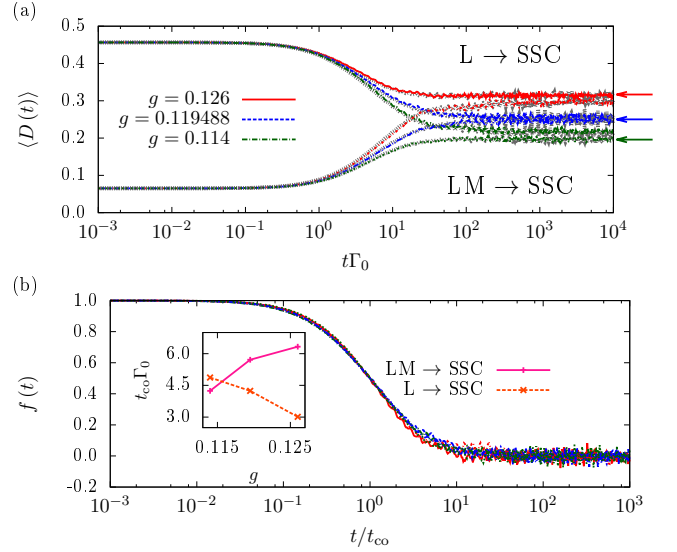


FIG. 9. (Color online) Real-time dynamics of the double occupancy  $\langle D(t) \rangle$  (colored curves) in the BFAM with the same parameters as in Fig. 6. Gray curves in the background show the corresponding double occupancy in the SIAM. Quenches from the L and LM starting points into the SSC phase. (a)  $\langle D(t) \rangle$  versus  $t\Gamma_0$ . (b) Data of BFAM quenches of (a) scaled via Eq. (26) versus  $t_{co}$ . Inset in (b) shows dependency of  $t_{co}$  on  $g$ .

### 4. Quenches between the LM and L phase

Starting from the LM phase and quenching into the L phase or vice versa are the two extremest types of quenches in the model. The results are depicted in Fig. 10(a) and Fig. 10(b) respectively. A steady-state value is approached which differs significantly from the equilibrium value and even stronger compared to quenching over one QCP.  $t_{co}$  is shown in the inset of Fig. 10(c) and is very similar in absolute value and functional dependency on  $g$  as in Fig. 8.

### 5. Short summary for the dynamics for F-type bath exponents

Our detailed analysis of the real-time dynamics with F-type bath exponents has demonstrated equilibration towards steady-state values which differ from the thermal equilibrium if the system is quenched into the L or the LM phase. We have also investigated the non-equilibrium dynamics using an effective SIAM defined by  $U_{ren}$  and could show that its dynamics reproduce exactly the one of the more complicated BFAM as exemplified in Fig. 6.

## B. B-type bath exponents

For bath exponents of the B-type  $(r, s) = (0.1, 0.6)$  the BFAM exhibits the same three phases but the critical

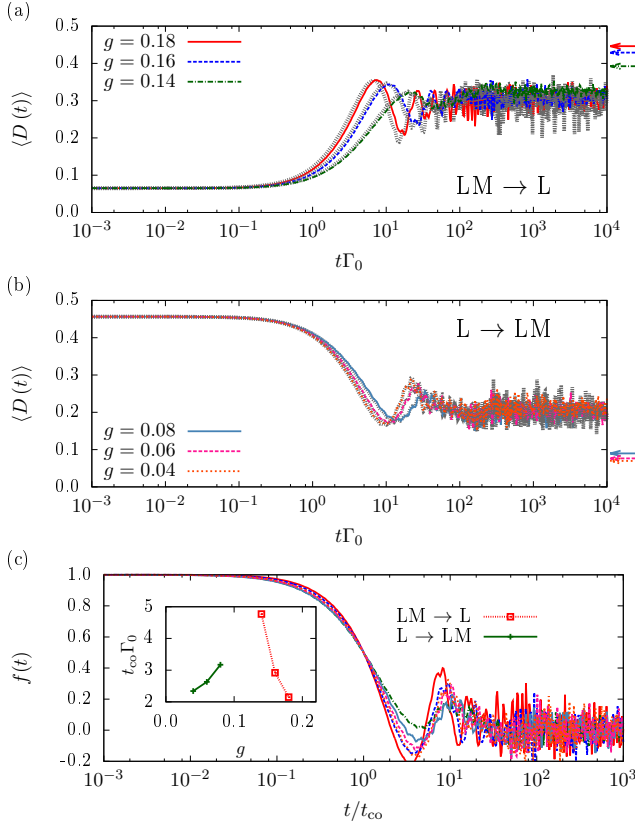


FIG. 10. (Color online) Real-time dynamics of the double occupancy  $\langle D(t) \rangle$  (colored curves) in the BFAM with the same parameters as in Fig. 6. Gray curves in the background show the corresponding double occupancy in the SIAM. (a) Quenches from the LM starting point into the L phase and vice versa in (b). (c) Scaled dynamics of all BFAM quenches via Eq. (26) versus the time scale  $t_{co}$ . Inset in (c) shows dependency of  $t_{co}$  on  $g$ .

exponents of the equilibrium thermodynamics are determined by the properties of the bosonic bath [20]. The question arises whether the non-equilibrium dynamics is also governed by the low-energy modes of bosonic bath or whether only an  $U_{ren}$  is generated and the dynamics follows an effective SIAM as for the F-type exponents.

Since we use the Coulomb repulsion  $U/\Gamma_0 = 1 < U_c/\Gamma_0$  for  $\Gamma_0/D = 0.01$  as in the case of F-type bath exponents, the BFAM can only access the SSC and L phase by varying over  $g$ . A larger Coulomb repulsion (not shown here) is needed to enter the LM phase being a mirror image of the L phase.

In the following we investigate three cases: (a) The BFAM and the effective SIAM are in the L phase requiring a very strong attractive Coulomb interaction in the SIAM and a large bosonic coupling in the BFAM. (b) For the same initial and final  $\langle D \rangle_{eq}$ , the BFAM is characterized by the L FP while the effective SIAM remains in SSC FP. (c) The real-time dynamics for both models are governed by the SSC FP.

Using the parameters stated in Tab. II, with the ini-

TABLE II. Correspondence between the bosonic coupling  $g$  of the B-type BFAM and the Coulomb repulsion  $U/\Gamma_0$  of the SIAM with respect to Eq. (25) and model parameters as described in the beginning of Sec. IV B.

Phase	$\langle D \rangle_{eq}$	$g$	$U/\Gamma_0$
<b>L</b>	<b>0.48729475</b>	<b>0.50</b>	<b>-30.5572</b>
(L in SIAM)	0.48601585	0.48	-27.7935
	0.48455407	0.46	-25.1727
	0.48287547	0.44	-22.6981
	0.48093136	0.42	-20.3643
<b>L</b>	<b>0.434957</b>	<b>0.25</b>	<b>-5.98</b>
(SSC in SIAM)	0.427673	0.24	-5.43
	0.418887	0.23	-4.84
	0.407986	0.22	-4.26
	0.276267	0.13	-0.533
	0.264578	0.12	-0.295
	0.253931	0.11	-0.079
<b>SSC</b>	<b>0.25</b>	<b>0.106</b>	<b>0</b>
(SSC in SIAM)	0.244341	0.10	0.115
	0.235799	0.09	0.286
	0.228286	0.08	0.439

tial conditions in bold, the real-time double occupancy  $\langle D(t) \rangle$  for these three cases are plotted in Fig. 11. The results for the BFAM are shown as colored curves while the corresponding data using the effective SIAM are depicted as gray curves in the background.

We start with quenches deep in the L phase with an initial value  $\langle D \rangle_{eq} \approx 0.49$  which indicates that the local spin states  $|\sigma\rangle$  are almost completely depopulated. This requires a strong bosonic couplings in the BFAM and a very large attractive  $U_{ren}$  in the SIAM. The corresponding real-time dynamics starting and ending at the same equilibrium expectation values  $\langle D \rangle_{eq}$  are shown in Fig. 11(a). Trivially, the starting and the end points are identical by construction. However, we observe clear differences in the dynamics in both models. The local decay minimum is much more pronounced in the SIAM while the additional low-energy bosonic modes lead to stronger damping at all times. Furthermore, the characteristic decay time is significantly longer in the BFAM. Here, the effect of the bosonic bath influences directly the dynamics and cannot be casted into a single parameter  $U_{ren}$ . Since the bosonic coupling is large the charge fluctuation scale  $\Gamma_0$  will be renormalized [49, 69, 87–89].

Setting  $t_0 = 0$  in Eq. (13) reduces the BFAM to the Anderson-Holstein model [88]. After decoupling the fermionic bad from the impurity, the remaining problem can be solved exactly via Lang-Firsov transformation [69, 87] leading to the formation of a polaron and a shifted harmonic oscillator. After applying the unitary Lang-Firsov transformation to the Anderson-Holstein model, the coupling to the fermionic bath  $H_{int,F}$  acquires additional factors by replacing

$$d_\sigma^\dagger \rightarrow \bar{d}_\sigma^\dagger = \bar{d}_\sigma^\dagger e^{-\frac{g_0}{\omega_0}(b_0^\dagger - b_0)} \quad (27)$$

where the operator  $\bar{d}_\sigma^\dagger$  creates a local polaron [49, 69, 87]

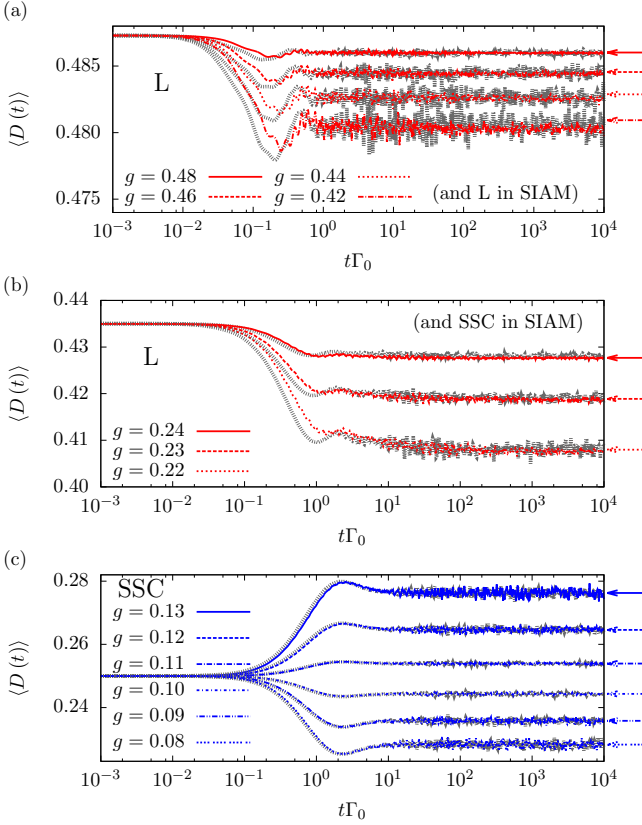


FIG. 11. (Color online) Real-time dynamics of the double occupancy  $\langle D(t) \rangle$  (colored curves) of the BFAM for bath exponents  $(r, s) = (0.1, 0.6)$  (B-type) with  $U/\Gamma_0 = 1$  and  $\Gamma_0/D = 0.01$ . Gray curves in the background are the corresponding double occupancy of the SIAM with  $\Gamma_0/D = 0.01$ . We perform quenches (a) deep within the L phase, where also the SIAM is in the L phase, (b) in the L phase of the BFAM, while the SIAM is in the SSC phase, and (c) within the SSC phase of both models.

This leads to a dynamic reduction of the bare hybridization strength to a value  $\Gamma_{\text{eff}}$  at very low temperature.  $\Gamma_{\text{eff}}$  depends on the RG flow, is iteration dependent [49] and only reaches a new constant value in the low-temperature fixed point. In the full BFAM, however, an additional energy or iteration dependency is generated by the bosonic bath neglected in the Anderson-Holstein model. For small  $g_0/\omega_0$  the renormalization can be neglected but for large values it can become relevant for the dynamics.

Consequently, we relate the fact that we have not been able to find a suitable set of parameters for the SIAM with  $\langle D_{\text{eq}}(U/\Gamma_0, D/\Gamma_0) \rangle = \text{const}$  and simultaneously maps the BFAM dynamics onto those of an effective SIAM to the energy-dependent renormalization [49, 89] of  $\Gamma_{\text{eff}}$  in the presence of bosonic modes.

The real-time dynamics in the BFAM depicted in Fig. 11(b) is governed by the L FP while for the same initial and final values  $\langle D \rangle_{\text{eq}}$  the dynamic in the effective SIAM is driven by the SSC FP: A mapping of the BFAM on the SIAM clearly fails and the comparison between

the quenches in the BFAM and the SIAM is less fruitful since one compares different quench types. We note, however, that the decay time in the BFAM is also significantly enhanced compared to the effective SIAM in this case which might be attributed to the reduction of the charge fluctuation scale  $\Gamma_{\text{eff}}$ .

Finally, we present the dynamics for quenches within the SSC phase for both models in Fig. 11(c). We start from the locally degenerated SSC FP, i.e. all four local states are equally occupied corresponding to  $U_{\text{ren}} = 0$  and change either the bosonic coupling in the BFAM or quench the corresponding  $U_{\text{ren}}$  as stated in Tab. II in the SIAM. Now, the dynamics of both models coincide again. Firstly, the bosonic coupling is significantly lower than in the regimes depicted in Fig. 11(a) and (b) leading to the much weaker renormalization of  $\Gamma_{\text{eff}}$ . Secondly, the dynamics in the SSC phase is more dominated by the itinerant nature of the low-energy excitations leading to the Kondo effect.

Note that also for all presented quenches with B-type bath exponents we always observe equilibration, and the additional bosonic environment leads to a stronger damping of the long-time finite size oscillations compared to the SIAM. Thermalization, however, is found for all SSC quenches and for L quenches as long as  $|g_f - g_i|$  is not too large.

### C. Real-time dynamics for the quenches out of an asymmetric phase

In the previous section we have demonstrated that the real-time dynamics can essentially be described by an effective SIAM for F-type bath exponents using the corresponding  $U_{\text{ren}}$  induced by the presence of the bosonic bath. For B-type exponents, we have observed derivations between the full dynamics and those of the effective SIAM for large bosonic coupling constants: The relevant time scales for the full dynamics are longer than the one of the effective SIAM due to the energy-dependent renormalization of  $\Gamma_{\text{eff}}$ .

For ph symmetry broken models, the different asymmetric FPs have been identified in Refs. [18, 20]. In

TABLE III. Set of final parameters for the quenches in Fig. 12 in presence of particle-hole symmetry  $\epsilon_d = -U/2$ .

$\langle D \rangle_{\text{eq}}$	Phase	$g$	$U/\Gamma_0$
0.4558	L	$0.2 > g_c$	-8
	L	$0.4 > g_c$	6
	SSC (SIAM)		-13.144
0.3977	SSC	$0.2 < g_c$	-2
	L	$0.4 > g_c$	11
	SSC (SIAM)		-6.223
0.2156	SSC	$0.2 < g_c$	4.6
	SSC	$0.4 < g_c$	15
	SSC (SIAM)		1.1753



this section, we will address the two questions: (i) How does the system evolve from a strongly ph-symmetry broken state when the propagation is governed by a ph-symmetric Hamiltonian  $H_f$ , and (ii) what are the differences between an effective SIAM and the full BFAM?

In order to focus on exemplifying those two questions, we restrict ourselves to the dynamics for a constant DOS ( $r = 0$ ) and set  $s = 0.6$ , hence we use B-type bath exponents. The low-temperature equilibrium phase of the BFAM with a broken ph symmetry is characterized by the asymmetric SC FP for all  $|U/\Gamma_0| > 0$  and all  $g \geq 0$ . Similar to the spin-boson model [9, 57] no quantum phase transition can occur in the symmetry broken state.

We prepare the system initially in the ph-symmetry broken state by applying  $|\epsilon_{d,i}/\Gamma_0| \gg 1$  mimicking a large positive or negative gate voltage in a quantum dot [90] which depletes or completely fills the local orbital. Then, we restore ph symmetry by quenching the system to  $\epsilon_{d,f} = -U_f/2$  instantaneously at  $t = 0$ . We leave  $U = \text{const}$  at any time and only investigate the difference between  $g_i = g_f$  and artificially switching on the interaction with the bosonic bath as well, i.e.  $g_i = 0 \rightarrow g_f > 0$ .

In order to compare the effect of different values of  $g_f$ , below  $g_f < g_c$  and above  $g_f > g_c$  the critical value, and to address the question of thermalization, we adjust the bare value of  $U$  such that for each set of parameters the same equilibrium double occupancy  $\langle D \rangle_{\text{eq}}$  is obtained for all  $H_f$ . The fermionic bath is for all calculations constantly coupled with  $\Gamma(t)/D = 0.01$ .

By appropriate choices of  $U$ , we can find two parameter pairs  $(g_f, U_f)_{1,2}$  for a given  $\langle D \rangle_{\text{eq}} = \text{const}$  such that both pairs belong to (i) the SSC phase, (ii) the L phase or (iii) are located in two different phases such that  $g_1 < g_c$  and  $g_2 > g_c$ . In addition, we determine  $U_{\text{ren}}$  for the SIAM such that the local thermodynamic expectation values are equal to those of the BFAM. The FP of  $H_f$ , however, is always the symmetric SC FP for the SIAM.

The real-time dynamics of  $\langle n_d(t) \rangle$  for the three representative equilibrium double occupancies  $\langle D \rangle_{\text{eq}} = \text{const}$  is shown in Figs. 12 and 14. Independent of the model parameters,  $\langle n_d \rangle_{\text{eq}} = 1$  due to ph symmetry. For each plot, we have used the two coupling constants  $g_1 = 0.2$  and  $g_2 = 0.4$ . The corresponding values for  $U$  in the three cases are summarized in Tab. III. Additionally we supplement the dynamics of  $\langle n_d(t) \rangle$  obtained with the effective SIAM for the same  $\langle D \rangle_{\text{eq}}$ ; for the  $U$  values see Tab. III.

We start with  $\langle D \rangle_{\text{eq}} \simeq 0.4558 > 1/4$  for all  $H_f$ , corresponding to  $U_{\text{ren}} < 0$  as stated in Tab. III. Both final values of  $g_f = 0.2, 0.4$  are located in the L phase of the BFAM. For each of the final couplings we either start from an initially decoupled bosonic bath ( $g_i = 0$ ) or the bosonic bath coupling remains unaltered ( $g_i = g_f$ ). The resulting real-time dynamics depicted in Fig. 12(a) reveals characteristic differences in the real-time dynamics: (i) the larger the coupling to the bosonic bath the larger

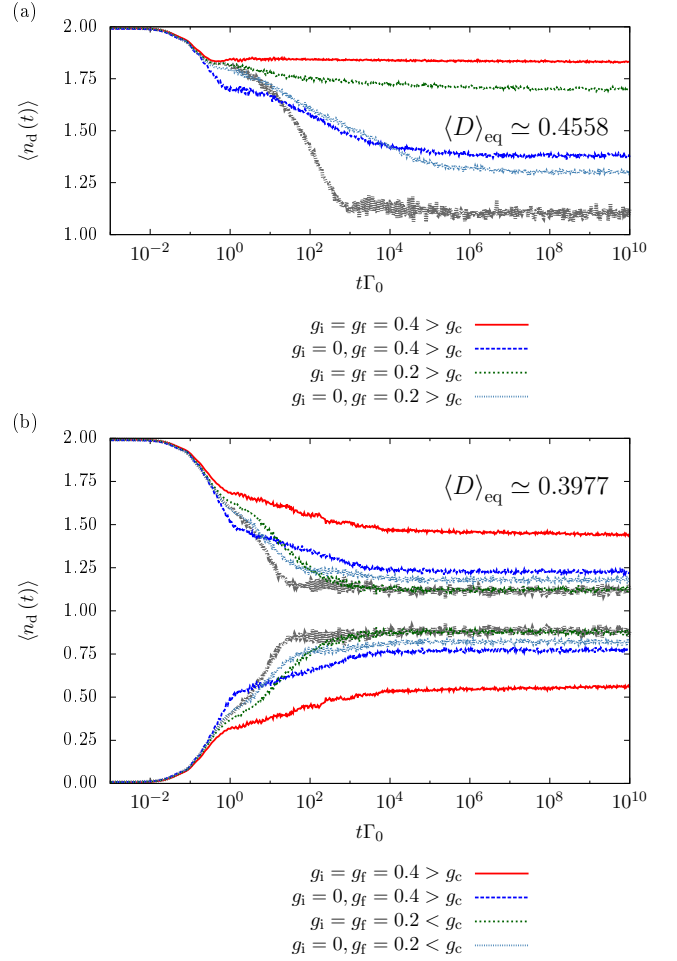


FIG. 12. (Color online) Dynamics of the level occupancy  $\langle n_d(t) \rangle$  of the BFAM with  $(r, s) = (0, 0.6)$  for quenches from ph asymmetry to ph symmetry at finite temperature  $T/D \sim 1.2 \cdot 10^{-7}$  for the equilibrium double occupancy (a)  $\langle D \rangle_{\text{eq}} \simeq 0.4558$  and (b)  $\langle D \rangle_{\text{eq}} \simeq 0.3977$ . NRG parameters are  $\Lambda = 6$ ,  $N_S = 800$ ,  $N_B = 8$ ,  $N_z = 8$  for the BFAM and changed to  $N_S = 2000$  for the SIAM.

the steady-state value of  $n_d^\infty$ ,

$$n_d^\infty = \lim_{T \rightarrow \infty} \frac{1}{T} \int_0^T dt \langle n_d(t) \rangle \quad , \quad (28)$$

and (ii) the bosonic system maintains its inertia for  $g = \text{const}$  suppressing the relaxation to the equilibrium expectation value even further. In order to illustrate the difference a gray shaded curve (color online) of the corresponding dynamics using the effective SIAM has been added for comparison.

Note that the short-time dynamics is identical for all three cases: The charge flow off the impurity is governed by the charge fluctuation scale  $\Gamma_0$ . After an initial  $t^2$  decay, a friction induced slowdown can be observed. In the localized phase, an effective DOF decouples from the rest of the bath, and therefore, its overlap with the initial state prevents the system to approach its equilibrium

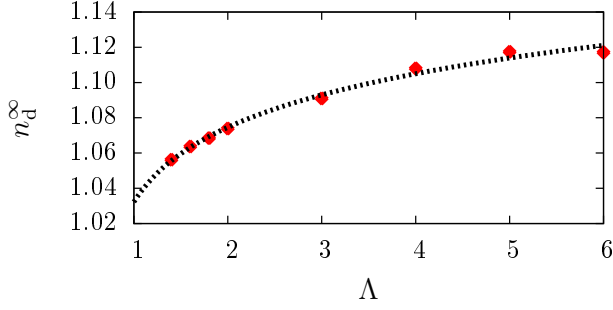


FIG. 13. (Color online)  $\Lambda$  dependence of  $n_d^\infty$  marked as rhombuses and calculated for the effective SIAM with  $U/\Gamma_0 = -6.223$  as used in Fig. 12(b). The dashed curve is an optimal fit curve extrapolating  $n_d^\infty$  in the limit  $\Lambda \rightarrow 1^+$ . NRG parameters as in Fig. 12.

value.

Our results agree with previous real-time investigations on the spin-boson model [41, 42] where in the localized phase the spin polarization is constant over a long stretch of time. However,  $\langle n_d(t) \rangle$  remains constant even for times  $t/T > 1$ , for the finite temperature  $T/D \sim 1.2 \cdot 10^{-7}$  of our calculations.

This indicates that also thermal fluctuations do not influence the long-time behavior of the level occupancy in contrary to the dynamics in the spin-boson model. We relate this behavior to the conservation laws of charge and spin which is absent in the spin-boson model. For the spin dynamics in the central spin model [91] it is known [92] that the existence of a non-decaying fraction of a spin-correlation function is related to conservation laws even in absence of integrability. The lower bound of the long-time limit could be estimated [92] by the application of the Mazur inequality [93]. In our case, however, the initial density matrix and the final states represent a complicated many-body problem that prevents us from a straight forward evaluation of a Mazur inequality in order to obtain an analytic estimate for the lower boundary of  $n_d^\infty$  depending on the initial conditions.

Choosing  $\langle D \rangle_{\text{eq}} \simeq 0.3977$  enables us to find two parameter pairs  $(g_f, U_f)$  such that for  $g_1 = 0.2$ ,  $H_f$  approaches the SSC FP while for  $g_2 = 0.4$ , we find a L FP in equilibrium.  $\langle n_d(t) \rangle$  is presented in Fig. 12(b) for those parameters. For all cases, the initial decay is governed by  $\Gamma_0$ , a steady state is found at long times, and the system equilibrates. Note that we present results on an exponentially long time scale not accessible to other methods.

For  $g_2 = 0.4 > g_c$ , the deviations to the thermal equilibrium are large and depend on the initial condition. For a constant coupling to the bosonic bath, the relaxation is significantly suppressed. For  $g_i = 0$ , however, the build up of correlations in the L phase needs some time and  $n_d^\infty$  is closer to the thermal value. For  $g_1 = 0.2 < g_c$ , the steady-state value agrees perfectly with those obtained from the effective SIAM. Data for the two complementary cases,  $n_d(t=0) \approx 0$  and  $n_d(t=0) \approx 2$  are shown to

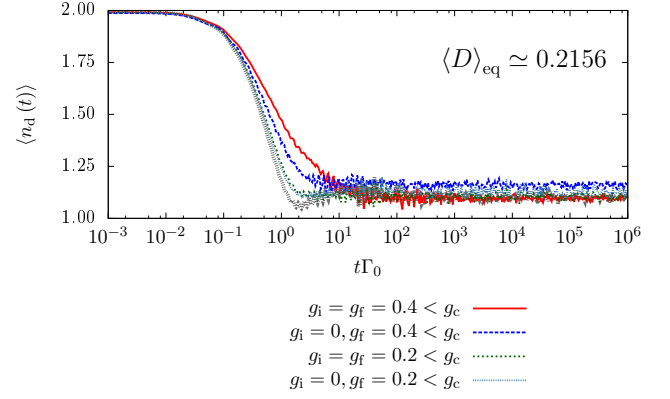


FIG. 14. (Color online) Dynamics of the level occupancy  $\langle n_d(t) \rangle$  of the BFAM with  $r = 0$  and  $s = 0.6$  for quenches from ph asymmetry to ph symmetry at finite temperature  $T/D \sim 1.2 \cdot 10^{-7}$  for  $\langle D \rangle_{\text{eq}} \simeq 0.2156$ . NRG parameters as in Fig. 12.

demonstrate the particle-hole symmetry of these curves.

Although, we notice a discrepancy between the steady-state value of  $n_d^\infty$  and its equilibrium value  $\langle n_d \rangle_{\text{eq}} = 1$ , we can conclude that the system is thermalizing in the SSC phase and the difference is a discretization artifact of the TD-NRG [41, 68, 76]. To prove this point, we have performed non-equilibrium calculations for identical model parameters but different values of  $\Lambda$ . The results are depicted in Fig. 13. Using a fit function, it becomes apparent that  $\lim_{\Lambda \rightarrow 1^+} n_d^\infty(\Lambda) = 1$  [94].

The results for the last case  $g_1, g_2 < g_c$  with  $\langle D \rangle_{\text{eq}} \simeq 0.2156$  are shown in Fig. 14 for  $\Lambda = 6$ . Within the numerical accuracy thermalization is found for all different parameters. Again, the initial decay is equal for all bosonic coupling constants and only governed by  $\Gamma_0$  as before. The steady-state value is found up to  $t\Gamma_0 = 10^{10}$  although only data up to  $t\Gamma_0 = 10^6$  are depicted in the figure. After a fast initial decay, we note a slowdown of the dynamics in the presence of a large coupling to the bosonic bath.

## V. CONCLUSION

In this paper we have investigated the influence of a bosonic bath onto the local non-equilibrium dynamics in the BFAM after a sudden change of parameters. The additional bosonic bath induces an additional attractive Coulomb interaction. We have defined a renormalized  $U_{\text{ren}}$  by equating the local double occupancy in the BFAM in the presence of a finite bath coupling and the bare value of  $U$  within an effective SIAM to estimate the  $U_{\text{ren}}$ .

We have shown that the real-time dynamics for F-type bath exponents can be fully understood within the effective SIAM defined by  $U_{\text{ren}}$  and the identical fermionic bath coupling function when ph symmetry is maintained



at all times. This includes quenches across the QCP into the localized phase, which also is found for a suitable  $U_{\text{ren}} < 0$ . There exist a one-to-one correspondence of the QPT between the spin Kondo effect and the local moment phase to the charge Kondo effect and the localized phase. The spin Kondo regime and the charge Kondo regime are adiabatically connected, and there exists one unique SSC FP with identical spin and charge moments,  $\mu_{\text{eff}}^2$  and  $Q_{\text{eff}}^2$  respectively. Within the numerical accuracy, we find perfect agreement between the dynamics in BFAM and those within the SIAM.

For B-type bath exponents a different picture emerges. Although the major effect of the bosonic bath is included into the renormalization  $U \rightarrow U_{\text{ren}}$ , the non-equilibrium dynamics of the full BFAM differs significantly to those of the effective SIAM. While for the quenches within the SSC phase the dynamics in both modes coincide, the mapping of the dynamics of the BFAM onto an effective SIAM fails for quenches within the L phase: Either in the effective SIAM the quench is of a different type, while the BFAM is already driven by the bosonic bath, or the bosonic coupling is very strong so that the characteristic time scale of the dynamics is increased in the BFAM compared to the dynamics in the SIAM.

Although all quenches equilibrate for long times to a steady-state value, thermalization is only found for quenches into the SSC phase or very close to the QCP where the characteristic low energy scale vanishes. With increasing distance to the QCP, the low-energy LM or L FP is approached faster in the NRG iterations, indicating a smaller spatial extension [39, 45, 46, 95] of the decoupled effective moment. Then, the difference between the steady-state value and the thermal equilibrium increases, since the local operators have a greater overlap with the decoupled local moments the larger the characteristic crossover energy scale to the low-temperature FP

becomes.

Furthermore, we have presented data for quenches from a ph-symmetry broken initial phase to a ph-symmetric state. There, we have restricted ourselves to  $r = 0$  and have focused only on the effect of an additional bosonic environment. In this case the LM phase is absent and the BFAM only shows a QPT between the SSC and the L phase.

The level occupancy  $\langle n_d(t) \rangle$  always approaches a steady-state value for all investigated parameter sets. Most strikingly, however,  $n_d^\infty$  deviates strongly from its thermodynamic equilibrium value, calculated with the final Hamiltonian, for quenches into the L phase ( $g > g_c$ ). This is related to a decoupling of an effective charge DOF from the bath continuum, preventing the local system to relax to the thermodynamic equilibrium. The magnitude of the deviation between the steady-state value and the equilibrium value depends on the initial condition. For an initially decoupled bosonic bath ( $g_i = 0$ ) the development of the localized charge DOF takes longer than the charge flow, and consequently, the difference is smaller compared to the case of  $g_i = g_f$ .

For quenches within the SSC phase,  $g < g_c$ , the dynamics of  $\langle n_d(t) \rangle$  in the BFAM and the effective SIAM are similar, although the presence of the bosonic coupling yields a slowdown of the relaxation process. Nevertheless,  $\langle n_d(t) \rangle$  thermalizes to its equilibrium value for long times in all cases  $g < g_c$ , which we have shown by an extrapolation of  $n_d^\infty(\Lambda)$  for  $\Lambda \rightarrow 1^+$ .

## ACKNOWLEDGMENTS

We would like to thank F. Güttge for his valuable contributions to the Bose-Fermi NRG code. We acknowledge financial support by the Deutsche Forschungsgemeinschaft through AN 275/7-1.

- 
- [1] R. Bulla, T. A. Costi, and T. Pruschke, *Rev. Mod. Phys.* **80**, 395 (2008).
  - [2] M. Nielsen and I. Chuang, *Quantum Computation and Quantum Information: 10th Anniversary Edition* (Cambridge University Press, 2010).
  - [3] K. G. Wilson, *Rev. Mod. Phys.* **47**, 773 (1975).
  - [4] H. R. Krishna-murthy, J. W. Wilkins, and K. G. Wilson, *Phys. Rev. B* **21**, 1003 (1980).
  - [5] H. R. Krishna-murthy, J. W. Wilkins, and K. G. Wilson, *Phys. Rev. B* **21**, 1044 (1980).
  - [6] R. Bulla, T. Pruschke, and A. C. Hewson, *Journal of Physics: Condensed Matter* **9**, 10463 (1997).
  - [7] C. Gonzalez-Buxton and K. Ingersent, *Phys. Rev. B* **57**, 14254 (1998).
  - [8] A. J. Leggett, S. Chakravarty, A. T. Dorsey, M. P. A. Fisher, A. Garg, and W. Zwerger, *Rev. Mod. Phys.* **59**, 1 (1987).
  - [9] R. Bulla, N.-H. Tong, and M. Vojta, *Phys. Rev. Lett.* **91**, 170601 (2003).
  - [10] R. Bulla, H.-J. Lee, N.-H. Tong, and M. Vojta, *Phys. Rev. B* **71**, 045122 (2005).
  - [11] M. Vojta, *Philosophical Magazine* **86**, 1807 (2006), <http://dx.doi.org/10.1080/14786430500070396>.
  - [12] G. R. Stewart, *Rev. Mod. Phys.* **73**, 797 (2001).
  - [13] M. Kirčán and M. Vojta, *Phys. Rev. B* **69**, 174421 (2004).
  - [14] M. T. Glossop and K. Ingersent, *Phys. Rev. Lett.* **95**, 067202 (2005).
  - [15] M. T. Glossop and K. Ingersent, *Phys. Rev. B* **75**, 104410 (2007).
  - [16] C.-H. Chung, M. T. Glossop, L. Fritz, M. Kirčán, K. Ingersent, and M. Vojta, *Phys. Rev. B* **76**, 235103 (2007).
  - [17] M. Glossop, N. Khoshkhou, and K. Ingersent, *Physica B: Condensed Matter* **403**, 1303 (2008), proceedings of the International Conference on Strongly Correlated Electron Systems.
  - [18] M. Cheng, M. T. Glossop, and K. Ingersent, *Phys. Rev. B* **80**, 165113 (2009).
  - [19] E. M. Nica, K. Ingersent, J.-X. Zhu, and Q. Si, *Phys.*

- Rev. B **88**, 014414 (2013).
- [20] J. H. Pixley, S. Kirchner, K. Ingersent, and Q. Si, Phys. Rev. B **88**, 245111 (2013).
- [21] F. D. M. Haldane, Phys. Rev. B **15**, 281 (1977).
- [22] F. D. M. Haldane, Phys. Rev. B **15**, 2477 (1977).
- [23] J. K. Freericks, Phys. Rev. B **48**, 3881 (1993).
- [24] Q. Si, S. Rabello, K. Ingersent, and J. L. Smith, Nature **413**, 804 (2001).
- [25] Q. Si, S. Rabello, K. Ingersent, and J. L. Smith, Phys. Rev. B **68**, 115103 (2003).
- [26] N. Grewe and F. Steglich, in *Handbook on the Physics and Chemistry of Rare Earths*, Vol. 14, edited by K. A. Gschneidner, Jr. and L. Eyring (North-Holland, Amsterdam, 1991) p. 343.
- [27] M. Sigrist, H. Tsunetsugu, and K. Ueda, Phys. Rev. Lett. **67**, 2211 (1991).
- [28] P. Coleman, Physica B: Condensed Matter **259–261**, 353 (1999).
- [29] M. A. Ruderman and C. Kittel, Phys. Rev. **96**, 99 (1954).
- [30] T. Kasuya, Progress of Theoretical Physics **16**, 45 (1956).
- [31] K. Yosida, Phys. Rev. **106**, 893 (1957).
- [32] P. Fazekas, *Lecture Notes on Electron Correlation and Magnetism*, Series in modern condensed matter physics (World Scientific, 1999).
- [33] J. Kondo, Prog. Theor. Phys **32**, 37 (1964).
- [34] S. Doniach, Physica B **91**, 231 (1977).
- [35] K. Le Hur, Phys. Rev. Lett. **92**, 196804 (2004).
- [36] M.-R. Li, K. Le Hur, and W. Hofstetter, Phys. Rev. Lett. **95**, 086406 (2005).
- [37] V. May and O. Kühn, *Charge and Energy Transfer Dynamics in Molecular Systems* (Wiley-VCH, Berlin, 2000).
- [38] S. Welack, M. Schreiber, and U. Kleinekathoefer, J. Chem. Phys. **124**, 044712 (2006).
- [39] K. G. Wilson, Rev. Mod. Phys. **47**, 773 (1975).
- [40] F. B. Anders and A. Schiller, Phys. Rev. Lett. **95**, 196801 (2005).
- [41] F. B. Anders and A. Schiller, Phys. Rev. B **74**, 245113 (2006).
- [42] F. B. Anders, R. Bulla, and M. Vojta, Phys. Rev. Lett. **98**, 210402 (2007).
- [43] D. Roosen, M. R. Wegewijs, and W. Hofstetter, Phys. Rev. Lett. **100**, 087201 (2008).
- [44] H. T. M. Nghiem and T. A. Costi, Phys. Rev. B **90**, 035129 (2014).
- [45] B. Lechtenberg and F. B. Anders, Phys. Rev. B **90**, 045117 (2014).
- [46] C. Kleine, J. Mußhoff, and F. B. Anders, Phys. Rev. B **90**, 235145 (2014).
- [47] F. B. Anders, Phys. Rev. Lett. **101**, 066804 (2008).
- [48] S. Schmitt and F. B. Anders, Phys. Rev. Lett. **107**, 056801 (2011).
- [49] A. Jovchev and F. B. Anders, Phys. Rev. B **87**, 195112 (2013).
- [50] L. Mühlbacher and E. Rabani, Phys. Rev. Lett. **100**, 176403 (2008).
- [51] T. L. Schmidt, P. Werner, L. Mühlbacher, and A. Komnik, Physical Review B (Condensed Matter and Materials Physics) **78**, 235110 (2008).
- [52] E. Gull, A. J. Millis, A. I. Lichtenstein, A. N. Rubtsov, M. Troyer, and P. Werner, Rev. Mod. Phys. **83**, 349 (2011).
- [53] M. Schiró and M. Fabrizio, Phys. Rev. B **79**, 153302 (2009).
- [54] K. F. Albrecht, H. Wang, L. Mühlbacher, M. Thoss, and A. Komnik, Phys. Rev. B **86**, 081412 (2012).
- [55] E. Y. Wilner, H. Wang, G. Cohen, M. Thoss, and E. Rabani, Phys. Rev. B **88**, 045137 (2013).
- [56] U. Schollwöck, Annals of Physics **326**, 96 (2011).
- [57] A. J. Leggett, S. Chakravarty, A. T. Dorsey, and M. P. A. Fisher, Rev. Mod. Phys. **59**, 1 (1987).
- [58] M. Vojta, N.-H. Tong, and R. Bulla, Phys. Rev. Lett. **102**, 249904(E) (2009).
- [59] M. Vojta, R. Bulla, F. Güttge, and F. Anders, Phys. Rev. B **81**, 075122 (2010).
- [60] M. Vojta, Phys. Rev. B **85**, 115113 (2012).
- [61] C. Li, D. Zhang, X. Liu, S. Han, T. Tang, C. Zhou, W. Fan, J. Koehne, J. Han, M. Meyyappan, A. M. Rawlett, D. W. Price, and J. M. Tour, Appl. Phys. Lett. **82**, 645 (2003).
- [62] Z. J. Donhauser, B. A. Mantooth, K. F. Kelly, L. A. Bumm, J. D. Monnell, J. J. Stapleton, D. W. Price, A. M. Rawlett, D. L. Allara, J. M. Tour, and P. S. Weiss, Science **292**, 2303 (2001).
- [63] M. Galperin, M. A. Ratner, and A. Nitzan, Journal of Physics: Condensed Matter **19**, 103201 (2007).
- [64] S. Hershfield, Phys. Rev. Lett. **70**, 2134 (1993).
- [65] P. W. Vigman and A. M. Finkelstein, Sov. Phys. JETP **78**, 102 (1978).
- [66] P. Schlottmann, Phys. Rev. B **22**, 613 (1980).
- [67] E. Eidelstein, D. Goberman, and A. Schiller, Phys. Rev. B **87**, 075319 (2013).
- [68] F. Güttge, F. B. Anders, U. Schollwöck, E. Eidelstein, and A. Schiller, Phys. Rev. B **87**, 115115 (2013).
- [69] G. Mahan, *Many-Particle Physics* (Plenum Press, New York, 1981).
- [70] P. W. Anderson, Phys. Rev. **124**, 41 (1961).
- [71] M. T. Glossop and D. E. Logan, Journal of Physics: Condensed Matter **15**, 7519 (2003).
- [72] D. Withoff and E. Fradkin, Phys. Rev. Lett. **64**, 1835 (1990).
- [73] U. Weiss, *Quantum Dissipative Systems*, Series in modern condensed matter physics (World Scientific, 1993).
- [74] R. Bulla, The European Physical Journal Special Topics **180**, 153 (2009).
- [75] S. Kirchner, K. Ingersent, and Q. Si, Phys. Rev. B **85**, 075113 (2012).
- [76] E. Eidelstein, A. Schiller, F. Güttge, and F. B. Anders, Phys. Rev. B **85**, 075118 (2012).
- [77] F. Güttge, F. B. Anders, U. Schollwöck, E. Eidelstein, and A. Schiller, Phys. Rev. B **87**, 115115 (2013).
- [78] T. A. Costi, A. C. Hewson, and V. Zlatic, Journal of Physics: Condensed Matter **6**, 2519 (1994).
- [79] R. Peters, T. Pruschke, and F. B. Anders, Phys. Rev. B **74**, 245114 (2006); A. Weichselbaum and J. von Delft, Phys. Rev. Lett. **99**, 076402 (2007).
- [80] M. Yoshida, M. A. Whitaker, and L. N. Oliveira, Phys. Rev. B **41**, 9403 (1990); W. C. Oliveira and L. N. Oliveira, *ibid.* **49**, 11986 (1994).
- [81] R. Bulla, M. T. Glossop, D. E. Logan, and T. Pruschke, Journal of Physics: Condensed Matter **12**, 4899 (2000).
- [82] K. Ingersent and Q. Si, Phys. Rev. Lett. **89**, 076403 (2002).
- [83] M. Vojta and L. Fritz, Phys. Rev. B **70**, 094502 (2004).
- [84] L. Fritz and M. Vojta, Phys. Rev. B **70**, 214427 (2004).
- [85] L. Fritz and M. Vojta, Reports on Progress in Physics **76**, 032501 (2013).
- [86] We like to note that the absolute value of  $t_{\text{co}}$  in our present study is roughly a factor of two greater compared

to the inset of Fig. 4(b) in Ref. [46]. This originates from the different value of  $\Lambda$  used in the present paper since we did not include the discretization correction factor  $A(\Lambda)$  in our calculation [4, 5].

- [87] I. G. Lang and Y. A. Firsov, JETP **16**, 1301 (1962).
- [88] A. C. Hewson and D. Meyer, J. Phys.: Condens. Matter **14**, 427 (2002).
- [89] E. Eidelstein, D. Goberman, and A. Schiller, Phys. Rev. B **87**, 075319 (2013).
- [90] J. M. Elzerman, R. Hanson, L. H. W. van Beveeren, B. Witkamp, L. M. K. Vandersypen, and L. P. Kouwenhoven, Nature **430**, 431 (2004).
- [91] M. Gaudin, J. Physique **37**, 1087 (1976).
- [92] G. S. Uhrig, J. Hackmann, D. Stanek, J. Stolze, and F. B. Anders, Phys. Rev. B **90**, 060301 (2014).
- [93] P. Mazur, Physica **43**, 533 (1969).
- [94] The small difference to  $n_d^\infty = 1$  is related to the finite number of state  $N_S$  used in each calculation.
- [95] V. Barzykin and I. Affleck, Phys. Rev. Lett. **76**, 4959 (1996).